



## Article

# Flexible Symmetric-Defection Antenna with Bending and Thermal Insensitivity for Miniaturized UAV

Xueli Nan <sup>1,2</sup>, Tongtong Kang <sup>1</sup>, Zhonghe Zhang <sup>3</sup>, Xin Wang <sup>1</sup> , Jiale Zhang <sup>1</sup> , Yusheng Lei <sup>4</sup>, Libo Gao <sup>4</sup>, Jianli Cui <sup>5,\*</sup> and Hongcheng Xu <sup>6,\*</sup>

- <sup>1</sup> School of Automation and Software Engineering, Shanxi University, Taiyuan 030006, China; nanxueli@sxu.edu.cn (X.N.); 202123603013@email.sxu.edu.cn (T.K.); 202123601010@email.sxu.edu.cn (X.W.); 202123603033@email.sxu.edu.cn (J.Z.)
- <sup>2</sup> School of Biomedical Engineering, Shanghai Jiao Tong University, Shanghai 200030, China
- <sup>3</sup> College of Electronics and Information Engineering, Shenzhen University, Shenzhen 518061, China; zzh422384683@163.com
- <sup>4</sup> Pen-Tung Sah Institute of Micro-Nano Science and Technology, Xiamen University, Xiamen 361102, China; 19920231151619@stu.xmu.edu.cn (Y.L.); lbgao@xmu.edu.cn (L.G.)
- <sup>5</sup> School of Physics and Electronics Engineering, Yuncheng University, Yuncheng 044000, China
- <sup>6</sup> School of Instrument Science and Technology, Xi'an Jiaotong University, Xi'an 710049, China
- \* Correspondence: cuijianli@ycu.edu.cn (J.C.); hongc187@outlook.com (H.X.);  
Tel.: +86-183-347-89099 (J.C.); +86-187-341-26627 (H.X.)

**Abstract:** Flexible conformal-enabled antennas have great potential for various developable surface-built unmanned aerial vehicles (UAVs) due to their superior mechanical compliance as well as maintaining excellent electromagnetic features. However, it remains a challenge that the antenna holds bending and thermal insensitivity to negligibly shift resonant frequency during conformal attachment and aerial flight, respectively. Here, we report a flexible symmetric-defection antenna (FSDA) with bending and thermal insensitivity. By engraving a symmetric defection on the reflective ground, the radiated unit attached to the soft polydimethylsiloxane (PDMS) makes the antenna resonate at the ISM microwave band (resonant frequency = 2.44 GHz) and conformal with a miniaturized UAV. The antenna is also insensitive to both the bending-conformal attachment (20 mm < r < 70 mm) and thermal radiation (20~100 °C) due to the symmetric peripheral-current field along the defection and the low-change thermal effect of the PDMS, respectively. Therefore, the antenna in a non-bending state almost keeps the same impedance matching and radiation when it is attached to a cylinder-back of a UAV. The flexible antenna with bending and thermal insensitivity will pave the way for more conformal or wrapping applications.

**Keywords:** antenna; flexible; bend; thermal; insensitivity



**Citation:** Nan, X.; Kang, T.; Zhang, Z.; Wang, X.; Zhang, J.; Lei, Y.; Gao, L.; Cui, J.; Xu, H. Flexible Symmetric-Defection Antenna with Bending and Thermal Insensitivity for Miniaturized UAV. *Micromachines* **2024**, *15*, 159. <https://doi.org/10.3390/mi15010159>

Academic Editor: Paulo M. Mendes

Received: 26 December 2023

Revised: 13 January 2024

Accepted: 19 January 2024

Published: 21 January 2024



**Copyright:** © 2024 by the authors. Licensee MDPI, Basel, Switzerland. This article is an open access article distributed under the terms and conditions of the Creative Commons Attribution (CC BY) license (<https://creativecommons.org/licenses/by/4.0/>).

## 1. Introduction

Flexible antennas with superior mechanical compliance as well as maintaining excellent electromagnetic (EM) features are widely attached to developable or undevelopable surfaces for various applications [1–5], such as wirelessly conformal communication [6], motion monitoring [7,8], power transmission [9], etc. Especially, antennas with strain insensitivity are flexible or stretchable which makes them possibly adaptable to diverse complex deformations [10–14]. For instance, liquid metal can be poured into PDMS microchannels to prepare antennas that can withstand tensile variations [15–17], and the two-dimensional serpentine structure can endow the antenna with stretchability [18]. However, flexibility is a double-edged sword that always provides limited or inconstant properties of the antenna during bending attachment [19–25]. Currently, alternative methods for this problem such as structural design and improved manufacturing technology can be used to achieve robust EM features of flexible antennas during deformation. For example, a symmetric-defection structure is used to make the flexible antenna suitable for bending deformation, however,

only for a large radius (100~200 mm) for multiple-input multiple-output (MIMO) applications [26]. Although the flexible antenna prepared by self-assembly technology effectively reduces the structure cracking or failure caused by deformation [27], the influence of bending and folding deformation on the EM feature for the antenna is also very obvious, and the fluctuation of performance is larger. Hence, there is an extreme need to tailor alternative antenna structures to offset bending impacts during deformation.

In addition, especially for long-term flight unmanned aerial vehicles (UAVs), ohm loss from inertial electrical components always causes some thermal interference, further weakening the antenna impedance matching [28]. Previous studies have verified the resonant frequency or working bandwidth shifts or mismatches with varying temperatures owing to the thermal sensitivity of the substrate [29–34]. For example, Tchafta et al. proposed a Rogers RT/duroid 5880-based copper antenna with 40.5 ppm/°C frequency changes in TM<sub>001</sub> mode [35] and Xu et al. used a CNT-based gas-permeable and resilient bowtie antenna to achieve 0.54 MHz/°C thermal sensitivity [36]. Mitradip et al. proposed a flexible temperature sensor with a sensitivity of ~1.2%/°C by a printed chipless poly(3,4-ethylenedioxythiophene):polystyrene (PEDOT:PSS)-based antenna [37]. For wireless sensors, the frequency shift from thermal variation, thus providing temperature sensing, is crucial, but thermal interference is negative for remoting communication antennas. Reports about methods or technology to eliminate thermal effects for antennas are rare. Therefore, it is greatly urgent to endow antennas with low heat sensitivity.

Here, we present a flexible symmetric-defection antenna (FSDA) with bending and thermal insensitivity. By engraving a symmetric-defection structure, the antenna performance can remain stable while withstanding bending deformation, and the low-change thermal effect of the PDMS material makes the antenna insensitive to temperature changes and it can be seamlessly conformal with undevelopable surfaces. The antenna achieves impedance matching at 2.44 GHz ( $S_{11} = -22$  dB) with a working bandwidth of 330 MHz and an omnidirectional radiation characteristic. Finally, the proposed FSDA maintains the same impedance matching and radiation while conformal with a miniaturized UAV, compared with the non-bending mode. This design provides a new idea for the study of conformal flexible antennas, which possibly represent potential applications for UAVs.

## 2. Design and Fabrication

### 2.1. Schematic and Design of the FSDA

The flexible antenna, which conforms with the vehicle surface of the UAV, is compact and has good aerodynamic properties [38–40], especially for operation between users and the base station at low altitude at the applied frequency band of ISM2.4 GHz [41–44], as shown in Figure 1a. The FSDA consists of the bottom symmetric-defection ground, the middle flexible dielectric substrate (PDMS,  $\epsilon_r = 2.65$ ,  $\tan\delta = 0.031$ ), and the top radiated unit (Figure 1b). Owing to the flexibility, the antenna can be seamlessly attached to the cylinder-back of a 3D-printed miniaturized UAV, as shown in Figure 1c. Figure 1d shows the process flow diagram of the antenna, in which a fast 355 nm UV laser with a power of 5 W at 50 kHz and a water-soluble tape (AQUASOL) are respectively used to engrave and transfer the copper-based structure. The laser-engraving and water-dissolving transferring method we adopted has vital advantages in the fabrication of various complex structures on the soft substrate and the speed (time consumption always < 1 min) for structure forming is superior to that of inkjet printing [45], screen printing [46], and 3D printing [47]. The equivalent circuit of the FSDA is shown in Figure 1e.  $Z_0$  is the intrinsic impedance, and the LC parallel resonant circuit consists of a symmetric-defection structure loaded on the ground plane, where the circular slot is regarded as the inductance ( $L$ ) and the middle gap is regarded as the capacitance ( $C$ ). The dimension of the symmetric-defection structure can be optimized to match the input impedance. To be insensitive to bending deformation and thermal radiation, the antenna should hinder the equivalent electric length change during attachment and maintain the stable dielectric effect, as shown in Figure 1f, thereby providing slight frequency shifting which is crucial for practical applications of UAVs.

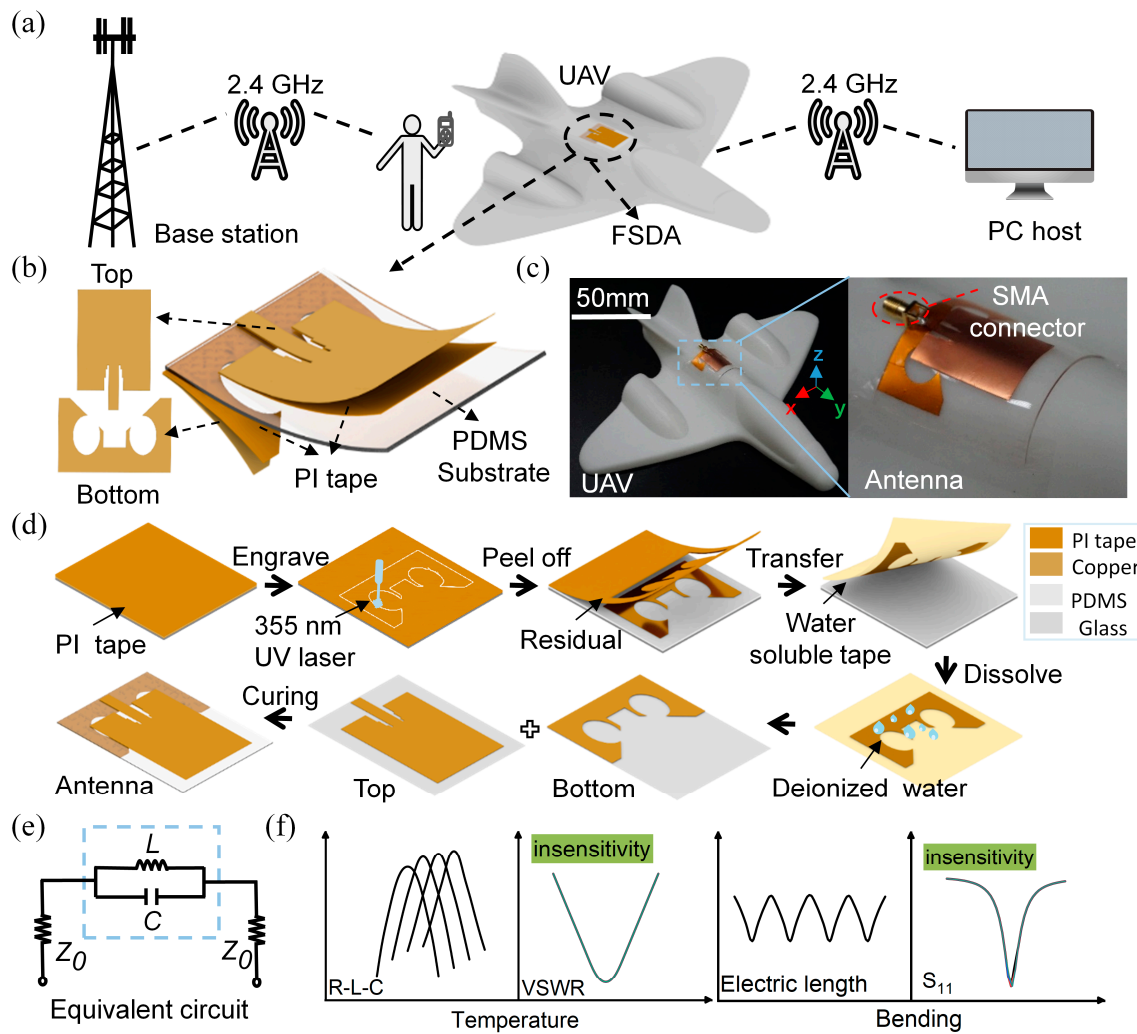


**Figure 1.** Rationale, design, and fabrication of the flexible symmetric-defection antenna (FSDA). (a) Wireless communication link between the FSDA attached to a UAV with radio frequency (RF) ends. (b) Three-dimensional structural illustration and its sectional view. (c) Photograph of the fabricated FSDA while it was conformal with a 3D-printed UAV model and the enlarged optical image. (d) Fabrication process of FSDA. (e) Equivalent RF resonant circuit. (f) Insensitive work rationale of the FSDA for thermal radiation and bending deformation.

### 2.2. Parameter Optimization of the FSDA

Based on the slot antenna and microstrip antenna principles [48–50], the resonant frequency of antennas highly relates to the equivalent electrical length and the dielectric constant of substrate layer as follows:

$$L_e = \frac{v_0}{2f_r\sqrt{\epsilon_r}} \quad (1)$$

where  $L_e$  is the equivalent electrical length of the microstrip antenna,  $v_0$  is the EM wave speed in vacuum,  $\epsilon_r$  is the dielectric constant of the substrate layer,  $f_r$  is the resonant frequency of the antenna. The length of the patch is usually  $\lambda_g/4$ , where  $\lambda_g$  is the working wavelength. We noted that the equivalent electrical length has a negative correlation with both  $\epsilon_r$  and  $f_r$  as shown in Figure 2a, in terms of Equation (1).

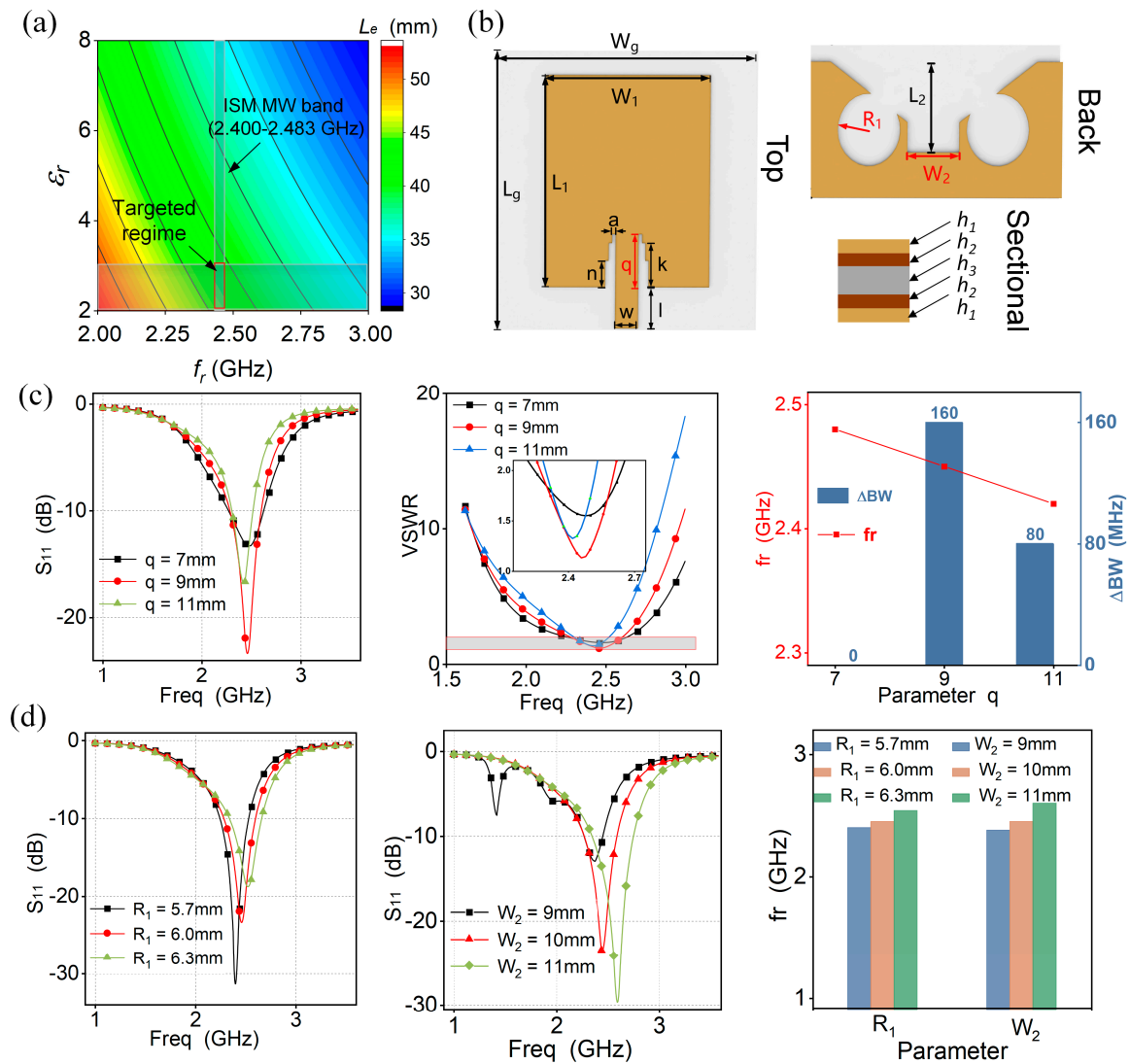


**Figure 2.** FSDA's structure and parameter optimization. (a) Analytical relationship of equivalent length between dielectric constant and resonant frequency. (b) Three structural views. (c,d) Parameter optimization in the return loss to  $q$ ,  $R_1$ , and  $W_2$ .

In order to achieve robust aerodynamics for UAVs' conformal antenna, a smaller electrical dimension effect provides low flight interference during long-term aircraft navigation at the ISM microwave band. Hence, the designed parameters in the inserted red rectangle are theoretically optimal for the simulated antenna. In addition, typically several soft materials [51,52], such as PDMS, TPU, and ecoflex silicone, have a dielectric constant of nearly 2~3. Further, according to the targeted regime, Figure 2b shows the designed structure dimension for the radiation unit and symmetric-defection ground. For a structural-defect microstrip antenna, the geometric dimension of the fed line and deflection are crucial parameters to alter the impedance matching. To further optimize the antenna dimension, the return loss and VSWR are related to the stepped slot length ( $q$ ), deflection-circle radius ( $R_1$ ), and their spacing ( $W_2$ ), as shown in Figure 2c,d. Utilizing the finite element analysis (FEA) method for multi-parameter optimization, we note that both the  $W_2$  and  $R_1$  mainly determine the resonant frequency shift, and the  $q$  has an impact on the working bandwidth and resonant depth. By optimizing these parameters, we eventually obtain a definite  $f_r$  and bandwidth. For an RF antenna device, when the return loss is less than  $-10$  dB, the fed port can match the radiation unit at the corresponding working frequency, achieving the lowest power loss. In addition, four different antennas (Figure S1a) were compared, and their re-

turn loss results are shown in Figure S1b. We found that the proposed symmetric-defection antenna with a deeper  $S_{11}$  at the resonant frequency and a wider working bandwidth compared with others achieves superior impedance matching. The symmetric balun feeding line at the radiation unit and the symmetric deflection at the ground make the antenna have deeper resonance and a wider working band. The final value of the geometric parameters of the FSDA is optimized, as shown in Table 1.

**Table 1.** Values of main parameters of the FSDA.

Parameter	Value (mm)
$L_g$	45
$W_g$	49.9
$L_1$	36
$W_1$	25
$l$	7
$w$	3.5
$h_1$	0.008
$h_2$	0.05
$h_3$	0.54
$a$	0.51
$n$	4.5
$k$	7.5
$q$	9
$R_1$	6
$L_2$	15
$W_2$	10

### 3. Results and Applications

#### 3.1. EM Performance of the FSDA

The simulation and measurement results of the proposed antenna in free space are shown in Figure 3. The FSDA is fed and measured by the Siglent vector network analyzer (VNA, SIGLENT SVA 1032X) as shown in Figure 3a and the result of  $S_{11}$  is plotted in Figure 3b. It can be seen that the antenna achieves good matching at the resonant frequency of 2.44 GHz with an  $S_{11}$  value of  $-22$  dB, and the working bandwidth is 330 MHz. The measured results are almost consistent with the simulation results ( $f_r = 2.45$  GHz,  $S_{11} = -23$  dB,  $BW = 330$  MHz). Figure 3c shows a good impedance match between the antenna and transmission line with an equivalent impedance of  $50 + j * 0$ , which helps to achieve highly efficient energy transmission. Figure 3d shows the near-field electric radiation, indicating a high-intensity electric field around the equivalent slotting edge in the FSDA. The 3D radiation field is shown in Figure 3e, and the peak gain at the resonance point is 1.6 dBi. The surface current distribution at 2.45 GHz is shown in Figure S2a. It is visible that the current is mainly concentrated at the microstrip line, the main radiation gap of the radiating patch, and the symmetric-deflection ground. And the currents on the radiating surface have similar flow paths around the edge of the patch, which is consistent with the theoretical prediction of the microstrip antenna edge radiation effect. Additionally, its radiation efficiency is 86% as shown in Figure S2b, verifying its excellent radiation capability. As shown in Figure 3f, the H-plane radiation pattern is a circle, and the E-plane directional pattern is in the shape of an “∞”, showing good standard slot-like antenna radiation properties and a great agreement between the measurement and simulation results, further verifying the accuracy and reliability of the antenna.

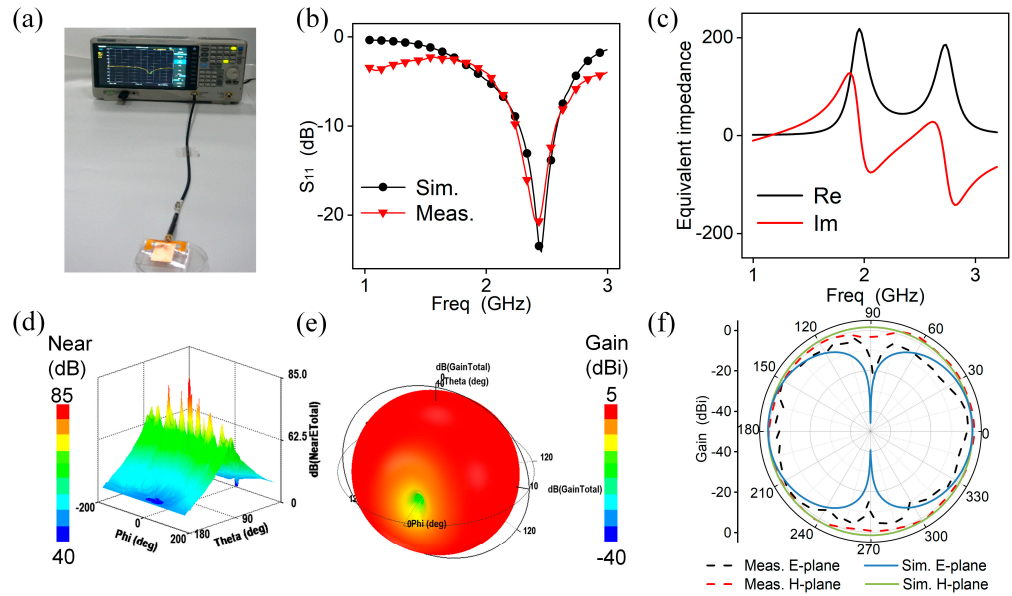


**Figure 3.** FSDA’s EM performance. (a) Test platform. (b) Simulated and measured  $S_{11}$  characteristics of the FSDA. (c) Equivalent impedance. (d) Near-field radiation. (e) Simulation result of 3D direction diagram. (f) Radiation patterns of H-plane and E-plane at resonant frequency when the antenna is in a flat state.

### 3.2. Thermal Insensitivity

A UAV’s antenna should withstand the impact of thermal radiation owing to ohm loss from inertial electrical components. Thermal radiation results in the anisotropic thermal expansion of the flexible substrate material, thus increasing or decreasing the dielectric constant, further forming a definite frequency shift as follows [35]:

$$\frac{\delta f_r}{f_r} = -\frac{1}{2} \frac{\delta \epsilon_r}{\epsilon_r} - \frac{\delta L_e}{L_e}, \quad (2)$$

$$\frac{\delta \epsilon_r}{\epsilon_r} = \alpha_{\epsilon_r} \delta T \quad (3)$$

where  $\frac{\delta f_r}{f_r}$  is the normalized frequency shift,  $\frac{\delta \epsilon_r}{\epsilon_r}$  is the normalized dielectric constant,  $\frac{\delta L_e}{L_e}$  is the normalized equivalent length,  $\alpha_{\epsilon_r}$  is the thermal coefficient of dielectric constant (TCDK) of the substrate along the length direction. As for the simulated frequency response versus the dielectric constant and the equivalent dimension, within a special frequency shift range (<0.5 GHz) for typical soft material ( $\epsilon_r = 2\sim 3$ ), the low thermal sensitivity of the antenna should focus on the inserted red targeted regime as shown in Figure 4a.

When the FSDA is connected with the VNA (Figure 4b), it is heated by a thermal radiation machine, and the  $S_{11}$  parameter is measured for the antenna at different temperatures (Figure S3). Figure 4c shows the measurement results of the  $S_{11}$  in the temperature range from 20~100 °C, indicating that the antenna maintains a low reflection loss and exhibits good thermal stability. Figure 4d,e depict the variations of resonant frequency ( $\Delta f_r$ ) and resonant depth with temperature, respectively. It can be seen that both the frequency shifting and resonance depth merely change at a negligible level (45 MHz and  $-4$  dB), demonstrating its thermal stability. To elucidate the thermal-stability rationale of the FSDA, the thermal–magnetic co-simulation by the FEA method is built at a temperature range from 20 to 100 °C as shown in Figure 4f. When the thermal-field vector is directed from the input (fed end) to the output port, we note that the thermal radiation majorly occurs near the fed line, with only a little at the back of the circle deflection (Figure 4g). This indicates that the thermal radiation can be attributed to ohm loss rather than EM radiation loss, and the volumetric heat-loss distribution of the FSDA further verified this property

(Figure 4h). Figure 4i plots a quantitative relationship between the EM loss and the temperature variation. A value of less than 10% (0.0143 W variation) further indicates the low thermal–magnetic effect of the FSDA for thermal interference, verifying the insensitivity of the FSDA to temperature changes.

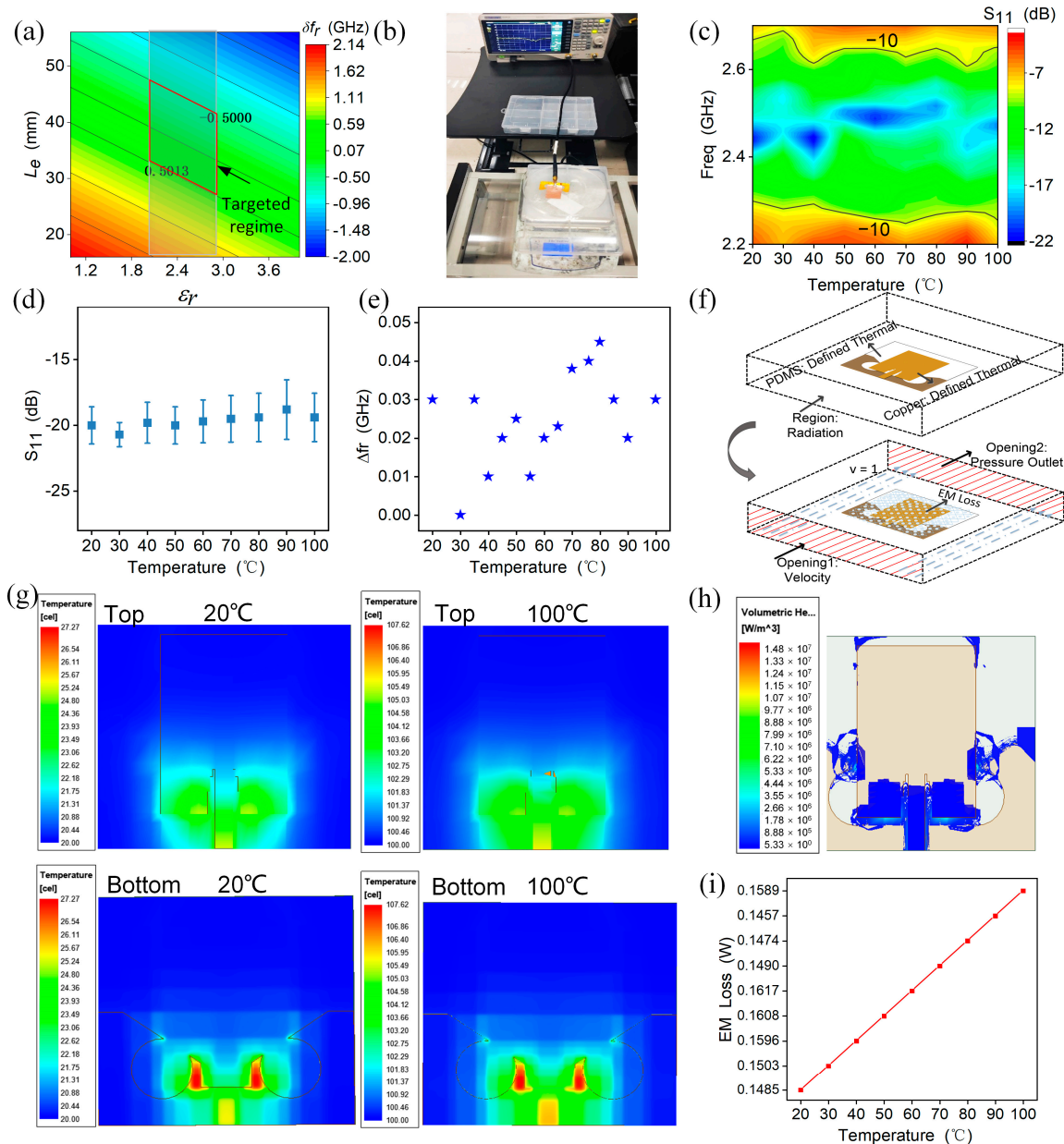


**Figure 4.** FSDA’s thermal-insensitivity verifications. (a) The relationship between normalized frequency shift and normalized dielectric constant and normalized equivalent length. (b) Temperature test platform. (c) Measured  $S_{11}$  result versus the frequency and temperature variations. (d,e) Variation of resonant frequency and resonant depth with temperature, respectively. (f) Schematic diagram of the thermal–magnetic co-simulation. (g) Thermal field of the FSDA under the thermal–magnetic coupling at 20 (left) and 100 °C (right). (h) Volumetric heat loss of the FSDA. (i) EM loss with varying temperatures.

### 3.3. Bending Insensitivity

To be insensitive to bending deformation, the antenna should hinder the equivalent electric length change during attachment by this symmetric-defection structure. Similarly, in order to adapt the designed antenna to an irregularly curved surface, we simulated

and measured the variation of return loss when the FSDA is attached to a cylinder with different radii (20~70 mm). Figure 5a shows the schematic diagram while the antenna conforms to the cylindrical surface. The simulated and measured results of  $S_{11}$  are shown in Figure 5b, where the results are almost consistent, with a good correlation in the target frequency band. The trends of resonant frequency and bandwidth with bending radius are shown in Figure 5c. The results reveal a small irregular shift in comparison to the flat state, as well as a slight increase in  $-10$  dB bandwidth but the antenna remains stable in the desired frequency range. In addition, different degrees of bending deformation can affect the radiation performance of the antenna, as shown in Figure S4. The radiation efficiency under bending states is 80~85%, which is less than 5% different from the radiation efficiency under flat states. This indicates that the antenna can still maintain a high radiation ability in bending states.

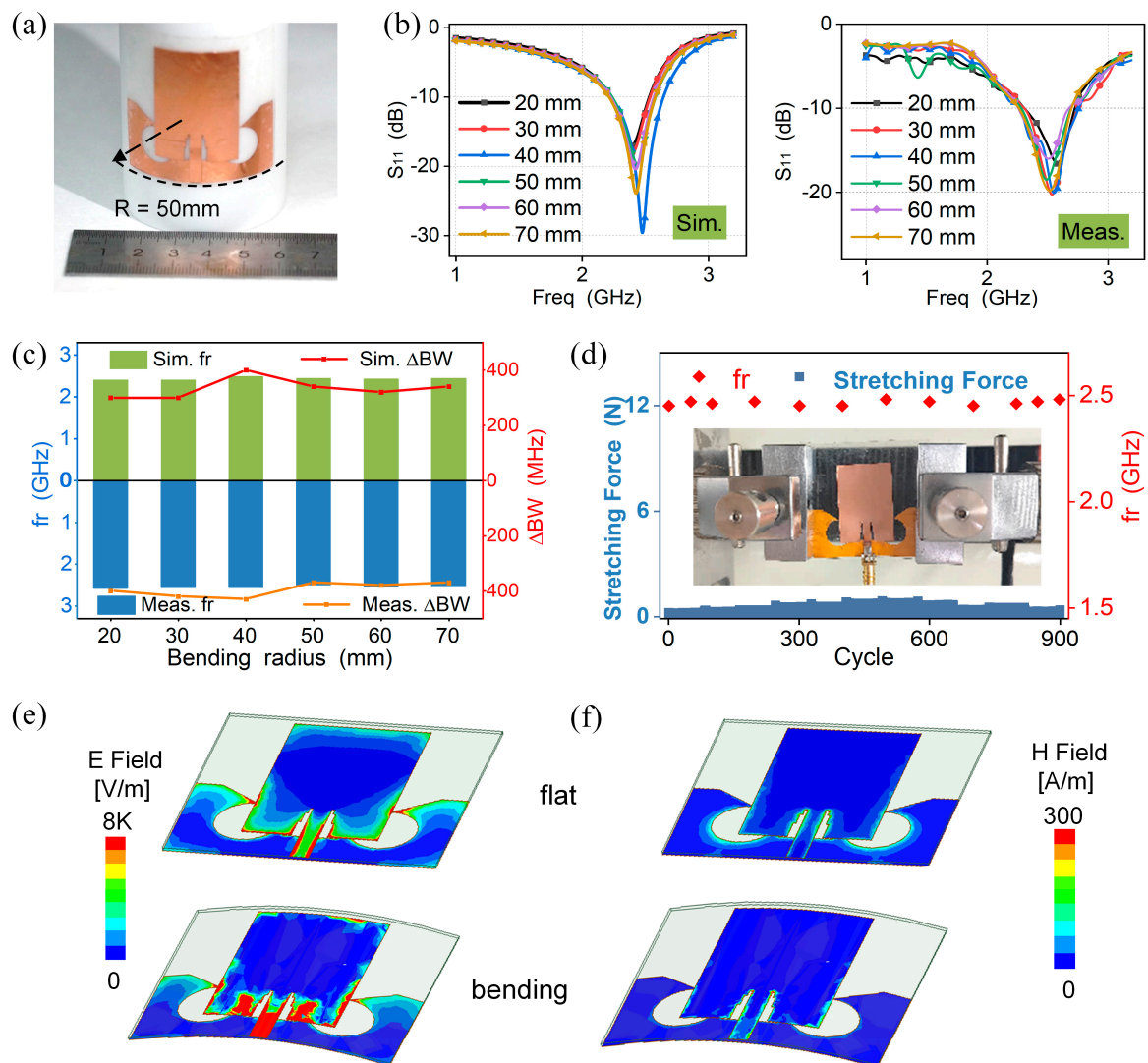


**Figure 5.** FSDA’s bending performance. (a) Bending conformity. (b) Simulated and measured results for  $S_{11}$  with different bending radii. (c) Variations of resonant frequency and bandwidth with bending radius. (d) Durability testing. (e,f) Electric and magnetic field comparison while the FSDA is flat (top) and bending (bottom).

We also conducted a uniaxial stretching test as shown in Figure S5a. We observe that the working bandwidth and resonant frequency of the antenna show negligible changes for stretching up to 4% ( $\Delta f_r < 10$  MHz,  $\Delta BW < 50$  MHz,  $|\Delta S_{11}| < 1$  dB, Figure S5b). This strain is attributed to the edge soft substrate instead of the copper-based antenna radiated

unit, which maintains stable impedance matching. Furthermore, to verify its long-term durability, the antenna was stretched for 900 bending cycles (Figure 5d). It was observed that the antenna still returned to its original state, with no significant change in resonant frequency, further showing its excellent long-term durability. To further elaborate on the radiation performance of the bending insensitivity, Figure 5e,f illustrate the electric and magnetic field distributions in the flat and bending states, respectively. The field patterns are almost consistent, and the symmetric-deflection ground concentrates more current, verifying that the symmetric-deflection ground is able to provide bending insensitivity for the FSDA by balancing the currents during bending deformation in EM radiation.

In addition, we tested the return loss when the FSDA is bent in the E-plane as shown in Figure S6a. We found that no observable frequency shifting occurs with the cylinder radius change, as shown in Figure S6b. According to the E-field and H-field (Figure S6c), the current distribution is almost consistent with that during the H-plane bending test, thus forming the negligible frequency shift. This is because the symmetric deflection on the ground concentrates more current, verifying that the symmetric-deflection ground provides bending insensitivity for the FSDA at the E-plane.

Also, the radiation pattern is carried out in the anechoic chamber far-field test system (KEYSIGHT E5071C, Dalian Dongshin Microwave, Dalian, China). Figure S7 shows the simulated and measured radiation patterns when the antenna is in the flat and bending states (50 mm and 70 mm). The radiation patterns during bending testing show good agreement with the results from the flat antenna, which further verifies the insensitivity of the antenna to bending deformation. The E-plane radiation patterns have little deviations that may be attributed to the antenna's installation error during the free space testing. These deviations are less than  $-20$  dBi, verifying its inferior interference to the co-polarization radiation.

### 3.4. Aircraft Applications of the FSDA

We have further analyzed the performance of the FSDA on the UAV. Here, the FSDA is measured and simulated separately on the flat and cylinder-back surfaces of the UAV (Figure 6a). To simulate the real conductive UAV surface, we attached a copper foil with a thickness of  $80\ \mu\text{m}$  to the 3D-printed UAV surface. The measurement results are shown in Figure S8. The resonant frequency almost remains constant and the working bandwidth ( $< -10$  dB) varies less than 10 MHz. These measurement results demonstrate that the proposed antenna can adapt to the UAV curved surface and has low sensitivity with more complex scenarios, which provides strong support for the further development of the flexible antenna in UAV applications. As can be seen in Figure 6b, when the antenna is fully attached to the cylinder-back of a 3D-printed miniaturized UAV (bending state), both the resonant frequency shift ( $\Delta f_r$ ) and working bandwidth change ( $\Delta BW$ ) at a negligible level ( $\Delta f_r = 70$  MHz and  $\Delta BW = 20$  MHz). Overall, the measured result highly correlates with the simulated results, which are also consistent with the results described in Figure 5. Figure 6c depicts the realized gain curve. The maximum realized gain is 1.64 dBi at 2.44 GHz while the FSDA is conformal with the UAV, which shows that the antenna has good radiation performance. The simulated radiation direction patterns for the E-plane and H-plane in two states are shown in Figure 6d and the 3D radiation pattern of the FSDA is shown in Figure 6e. It is obvious that the bending has almost no effect on the radiation direction pattern and it still exhibits an omnidirectional radiation characteristic in the H-plane. Compared with previous literature, our antenna exhibits a lower relative bending frequency shift (2.8%, defined as  $\frac{|F_{bending} - F_{flat}|}{F_{flat}}$  %), narrow return loss variation of only 1 dB, and 2% change in radiation efficiency as well as 4 dB change in thermal interference [27,37,53–60], as shown in Table 2. The above results fully demonstrate the reliability and effectiveness of the antenna in UAV communication systems.

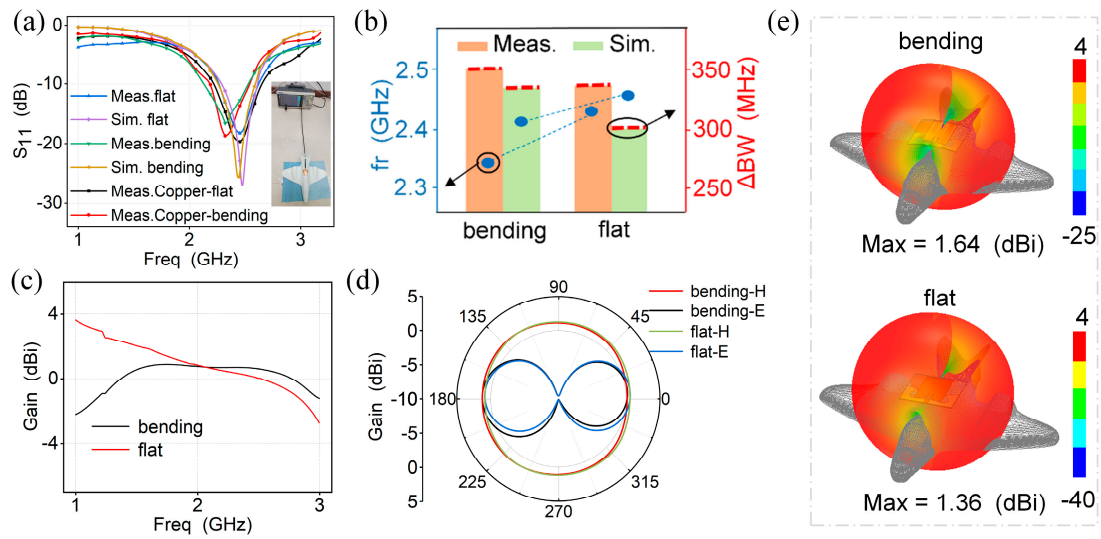


**Figure 6.** Applications of the FSDA with a no-load (flat) and bending state while attached to a UAV. (a) Comparison of simulated and measured  $S_{11}$  results. (b) Comparison of resonant frequency and bandwidth. (c) Gain curves with variation in frequency. (d) Radiation patterns of the H-plane and E-plane. (e) The 3D radiation pattern.

**Table 2.** Comparison of bending and thermal insensitivity of antennas.

Ref.	Flat				Bending							Thermal
	$f_r$ (GHz)	$S_{11}$ (dB)	$\Delta BW$ (MHz)	Efficiency (%)	Radius/Angle	$\frac{ F_{bending} - F_{flat} }{F_{flat}}$ (%)	$ \Delta S_{11} $ (dB)	$ \Delta BW $ (MHz)	Efficiency (%)	Durability		
[27]	2.32	-28	760	NA	40 (mm)	3%	10.84	310	NA	NA	NA	
[37]	1.2/5.8	-13/-20	220/4000	NA	$S_{11} > -10$ dB at lateral bending, mismatching					NA	NA	~20% at 5.8 GHz
[53]	2.4	-21	275	25.8%	25 (mm)	4.4%	3	65	27.5%	NA	NA	
[54]	2.45/5	-24/-14	170/700	37%/44%	28	2.1%	6/10	80/200	32%/36%	✓	NA	
[55]	2.53	-15	350	42.3%	70 (mm)	3.3%	2	190	NA	NA	NA	
[56]	2.45	-22	128	30.5%	60°	0.4%	10	20	27.9%	NA	NA	
[57]	5.7	-50	1600	80%	43	1.8%	24	100	83.5%	✓	NA	
[58]	2.43	-33	260	NA	40°	2%	19	80	NA	NA	NA	
[59]	2.47	-21	250	83%	30 (mm)	3.6%	8	100	70%	NA	NA	
[60]	2.43	-42	50	NA	43.2	0.8%	19	5	NA	✓	NA	
This work	2.45	-22	330	86%	40 (mm)	2.8%	1	100	84%	✓	$ \Delta BW _{max} \sim 45$ MHz, $ \Delta S_{11} _{max} \sim 4$ dB	

✓ yes; NA not applicable.

### 4. Conclusions

In this work, a flexible symmetric-defection antenna was proposed for miniaturized UAV applications in the ISM microwave band. The antenna consists of a radiating unit, a symmetric-defection ground structure, and a PDMS substrate. An engraving–transferring method for the fabrication of a flexible antenna is low-cost and environmentally friendly compared with conventional PCB manufacturing process. The antenna achieves the resonant frequency at 2.44 GHz ( $S_{11} = -22$  dB) with a working bandwidth of 330 MHz and omnidirectional radiation. The symmetric-defection ground balances current flowing during EM radiation as bending deformation and the PDMS-based substrate just provides a low-change thermal effect. Therefore, the proposed FSDA is highly flexible and insensitive to bending deformation and thermal radiation, making it suitable for applications in airborne devices such as UAVs. This antenna with bending and thermal insensitivity may be further optimized and integrated with various UAVs for high-fidelity communications.

**Supplementary Materials:** The following supporting information can be downloaded at: <https://www.mdpi.com/article/10.3390/mi15010159/s1>, Figure S1: (a) Four antennas with different structure designs. (b) Return loss of four antennas, Figure S2: (a) Surface current distribution of FSDA at 2.45 GHz. (b) Radiation efficiency, Figure S3: Return loss changes versus the temperature, Figure S4: Radiation efficiency at various bending radii and flat states, Figure S5: FSDA's stretching performance. (a) Stretching control machine. (b) Return loss changes in the FSDA versus different stretching strains, Figure S6: FSDA's bending performance (E-plane). (a) Optical image when the FSDA is attached to a cylinder surface along with the circumference direction. (b) Measured results for S11 with different bending radii. (c) Electric and magnetic field comparison while the FSDA is flat (top) and bending (bottom), Figure S7: Comparison of the radiation patterns. (a) Schematic illustration of the free space testing. (b) Optical image of the tested antenna on a rotating platform in the anechoic chamber. (c) Measured and simulated radiation patterns at the H-plane and E-plane of the FSDA under three states, flat (left), conformal cylinder with a radius of 50 mm (middle), and 70 mm (right), Figure S8: Measured results for the return loss while the antenna is tested with different states and an optical image of the antenna mounted on the copper-covered 3D-printed UAV.

**Author Contributions:** Conceptualization, X.N., T.K. and H.X.; methodology, T.K.; software, T.K.; validation, X.N., T.K. and H.X.; formal analysis, T.K.; investigation, T.K.; resources, T.K.; data curation, T.K.; writing—original draft preparation, T.K.; writing—review and editing, X.N., T.K., Z.Z., X.W., J.Z., Y.L., L.G., J.C. and H.X.; supervision, X.N., J.C. and H.X.; project administration, X.N. and L.G.; funding acquisition, X.N. and L.G. All authors have read and agreed to the published version of the manuscript.

**Funding:** This research was supported by the National Natural Science Foundation of China (No. 61804090, No. 62274140), the Fundamental Research Funds for the Central Universities (20720230030), and the Xiaomi Young Talents Program/Xiaomi Foundation.

**Data Availability Statement:** The data that support the findings of this study are available on request from the author (X.N.) upon reasonable request.

**Conflicts of Interest:** The authors declare no conflicts of interest.

## References

- Jia, Q.; Xu, H.; Xiong, M.F.; Zhang, B.; Duan, J. Omnidirectional Solid Angle Beam-Switching Flexible Array Antenna in Millimeter Wave for 5G Micro Base Station Applications. *IEEE Access* **2019**, *7*, 157027–157036. [[CrossRef](#)]
- Kirtania, S.G.; Elger, A.W.; Hasan, M.R.; Wisniewska, A.; Sekhar, K.; Karacolak, T.; Sekhar, P.K. Flexible Antennas: A Review. *Micromachines* **2020**, *11*, 847. [[CrossRef](#)] [[PubMed](#)]
- Xie, Z.; Avila, R.; Huang, Y.; Rogers, J.A. Flexible and Stretchable Antennas for Biointegrated Electronics. *Adv. Mater.* **2019**, *32*, e1902767. [[CrossRef](#)] [[PubMed](#)]
- Xu, H.; Zhang, B.-Z.; Duan, J.-P.; Cui, J.; Xu, Y.; Tian, Y.; Yan, L.; Xiong, M.; Jia, Q. Wide Solid Angle Beam-Switching Conical Conformal Array Antenna With High Gain for 5G Applications. *IEEE Antennas Wirel. Propag. Lett.* **2018**, *17*, 2304–2308. [[CrossRef](#)]
- Zhao, W.; Ni, H.; Ding, C.; Liu, L.; Fu, Q.; Lin, F.; Tian, F.; Yang, P.; Liu, S.; He, W.; et al. 2D Titanium carbide printed flexible ultrawideband monopole antenna for wireless communications. *Nat. Commun.* **2023**, *14*, 278. [[CrossRef](#)] [[PubMed](#)]
- Faisal, F.; Amin, Y.; Cho, Y.; Yoo, H. Compact and Flexible Novel Wideband Flower-Shaped CPW-Fed Antennas for High Data Wireless Applications. *IEEE Trans. Antennas Propag.* **2019**, *67*, 4184–4188. [[CrossRef](#)]
- Bhattacharjee, S.; Maity, S.; Chaudhuri, S.R.B.; Mitra, M. A Compact Dual-Band Dual-Polarized Omnidirectional Antenna for On-Body Applications. *IEEE Trans. Antennas Propag.* **2019**, *67*, 5044–5053. [[CrossRef](#)]
- Sindhu, B.; Kothuru, A.; Sahatiya, P.; Goel, S.; Nandi, S. Laser-Induced Graphene Printed Wearable Flexible Antenna-Based Strain Sensor for Wireless Human Motion Monitoring. *IEEE Trans. Electron Devices* **2021**, *68*, 3189–3194. [[CrossRef](#)]
- Li, H.; Sun, S.; Wang, B.; Wu, F. Design of Compact Single-Layer Textile MIMO Antenna for Wearable Applications. *IEEE Trans. Antennas Propag.* **2018**, *66*, 3136–3141. [[CrossRef](#)]
- Lee, Y.-H.; Lim, E.-H.; Bong, F.-L.; Chung, B.-K. Bowtie-Shaped Folded Patch Antenna With Split Ring Resonators for UHF RFID Tag Design. *IEEE Trans. Antennas Propag.* **2019**, *67*, 4212–4217. [[CrossRef](#)]
- Boyuan, M.; Pan, J.; Wang, E.; Luo, Y. Conformal Bent Dielectric Resonator Antennas With Curving Ground Plane. *IEEE Trans. Antennas Propag.* **2019**, *67*, 1931–1936. [[CrossRef](#)]
- Zhang, J.; Zhang, L.; Wang, Y.; Wang, Y.; Wang, C. Flexible kirigami with local cylindrical shell design for stretchable microstrip antenna. *Compos. Struct.* **2022**, *296*, 115879. [[CrossRef](#)]
- Alemaryeen, A.; Noghianian, S. On-Body Low-Profile Textile Antenna With Artificial Magnetic Conductor. *IEEE Trans. Antennas Propag.* **2019**, *67*, 3649–3656. [[CrossRef](#)]

14. Kim, Y.-S.; Basir, A.; Herbert, R.; Kim, J.; Yoo, H.; Yeo, W.-H. Soft Materials, Stretchable Mechanics, and Optimized Designs for Body-Wearable Compliant Antennas. *ACS Appl. Mater. Interfaces* **2019**, *12*, 3059–3067. [[CrossRef](#)] [[PubMed](#)]
15. Hayes, G.J.; Ju-Hee, S.; Qusba, A.; Dickey, M.D.; Lazzi, G. Flexible Liquid Metal Alloy (EGaIn) Microstrip Patch Antenna. *IEEE Trans. Antennas Propag.* **2012**, *60*, 2151–2156. [[CrossRef](#)]
16. Shi, C.; Zhigang, W.; Hallbjorner, P.; Hjort, K.; Rydberg, A. Foldable and Stretchable Liquid Metal Planar Inverted Cone Antenna. *IEEE Trans. Antennas Propag.* **2009**, *57*, 3765–3771. [[CrossRef](#)]
17. Sallam, M.O.; Kandil, S.M.; Volski, V.; Vandebosch, G.A.E.; Soliman, E.A. Wideband CPW-Fed Flexible Bow-Tie Slot Antenna for WLAN/WiMax Systems. *IEEE Trans. Antennas Propag.* **2017**, *65*, 4274–4277. [[CrossRef](#)]
18. Kanagasabai, M.; Sambandam, P.; Alsath, M.G.N.; Palaniswamy, S.; Ravichandran, A.; Girinathan, C. Miniaturized Circularly Polarized UWB Antenna for Body Centric Communication. *IEEE Trans. Antennas Propag.* **2022**, *70*, 189–196. [[CrossRef](#)]
19. Altinozen, E.; Vukovic, A.; Sewell, P. Assessment of the Robustness of Flexible Antennas to Complex Deformations. *IEEE Trans. Antennas Propag.* **2023**, *71*, 4714–4723. [[CrossRef](#)]
20. Jiang, Z.H.; Cui, Z.; Yue, T.; Zhu, Y.; Werner, D.H. Compact, Highly Efficient, and Fully Flexible Circularly Polarized Antenna Enabled by Silver Nanowires for Wireless Body-Area Networks. *IEEE Trans. Biomed. Circuits Syst.* **2017**, *11*, 920–932. [[CrossRef](#)]
21. Arif, A.; Zubair, M.; Ali, M.; Khan, M.U.; Mehmood, M.Q. A Compact, Low-Profile Fractal Antenna for Wearable On-Body WBAN Applications. *IEEE Antennas Wirel. Propag. Lett.* **2019**, *18*, 981–985. [[CrossRef](#)]
22. Sid, A.; Cresson, P.-Y.; Joly, N.; Braud, F.; Lasri, T. A flexible and wearable dual band bio-based antenna for WBAN applications. *AEU—Int. J. Electron. Commun.* **2022**, *157*, 154412. [[CrossRef](#)]
23. Sayem, A.S.M.; Simorangkir, R.B.V.B.; Esselle, K.P.; Hashmi, R.M.; Liu, H. A Method to Develop Flexible Robust Optically Transparent Unidirectional Antennas Utilizing Pure Water, PDMS, and Transparent Conductive Mesh. *IEEE Trans. Antennas Propag.* **2020**, *68*, 6943–6952. [[CrossRef](#)]
24. Zhang, S.; Zhu, J.; Zhang, Y.; Chen, Z.; Song, C.; Li, J.; Yi, N.; Qiu, D.; Guo, K.; Zhang, C.; et al. Standalone stretchable RF systems based on asymmetric 3D microstrip antennas with on-body wireless communication and energy harvesting. *Nano Energy* **2022**, *96*, 107069. [[CrossRef](#)]
25. Song, L.; Rahmat-Samii, Y. A Systematic Investigation of Rectangular Patch Antenna Bending Effects for Wearable Applications. *IEEE Trans. Antennas Propag.* **2018**, *66*, 2219–2228. [[CrossRef](#)]
26. Li, W.; Hei, Y.; Grubb, P.M.; Shi, X.; Chen, R.T. Compact Inkjet-Printed Flexible MIMO Antenna for UWB Applications. *IEEE Access* **2018**, *6*, 50290–50298. [[CrossRef](#)]
27. Liu, Y.; Wang, Z.-L.; Cang, D.-Y.; Gong, J.-S.; Qu, H.-W. A polyimide-based flexible monopole antenna. *J. Mater. Sci. Mater. Electron.* **2022**, *33*, 1686–1702. [[CrossRef](#)]
28. Mahfuz, M.M.H.; Park, C.-W. Review of Patch Antennas used in Drone Applications. *IEEE Access* **2023**, *11*, 58367–58388. [[CrossRef](#)]
29. Yao, J.; Mbanya Tchafa, F.; Jain, A.; Tjuatja, S.; Huang, H. Far-Field Interrogation of Microstrip Patch Antenna for Temperature Sensing Without Electronics. *IEEE Sens. J.* **2016**, *16*, 7053–7060. [[CrossRef](#)]
30. Tchafa, F.M.; Huang, H. Microstrip patch antenna for simultaneous temperature sensing and superstrate characterization. *Smart Mater. Struct.* **2019**, *28*, 105009. [[CrossRef](#)]
31. Sanders, J.W.; Yao, J.; Huang, H. Microstrip Patch Antenna Temperature Sensor. *IEEE Sens. J.* **2015**, *15*, 5312–5319. [[CrossRef](#)]
32. Miao, F.; Tian, P.; Tao, B.; Zang, Y. Passive RFID microstrip antenna sensor for temperature monitoring. *Vacuum* **2022**, *201*, 111108. [[CrossRef](#)]
33. Xu, H.; Cui, J.; Duan, J.; Zhang, B.; Tian, Y. Versatile Conical Conformal Array Antenna Based on Implementation of Independent and Endfire Radiation for UAV Applications. *IEEE Access* **2019**, *7*, 31207–31217. [[CrossRef](#)]
34. Kou, H.; Yang, L.; Zhang, X.; Shang, Z.; Shi, J.; Wang, X. Wireless Passive Microwave Antenna-Integrated Temperature Sensor Based on CSRR. *Micromachines* **2022**, *13*, 621. [[CrossRef](#)] [[PubMed](#)]
35. Tchafa, F.M.; Huang, H. Microstrip patch antenna for simultaneous strain and temperature sensing. *Smart Mater. Struct.* **2018**, *27*, 065019. [[CrossRef](#)]
36. Xu, H.; Zheng, W.; Yuan, Y.; Xu, D.; Qin, Y.; Zhao, N.; Duan, Q.; Jin, Y.; Wang, Y.; Wang, W.; et al. Flexible Gas-Permeable and Resilient Bowtie Antenna for Tensile Strain and Temperature Sensing. *IEEE Internet Things J.* **2022**, *9*, 23215–23223. [[CrossRef](#)]
37. Bhattacharjee, M.; Nikbakhtnasrabadi, F.; Dahiya, R. Printed Chipless Antenna as Flexible Temperature Sensor. *IEEE Internet Things J.* **2021**, *8*, 5101–5110. [[CrossRef](#)]
38. Wei, Z.; Junfeng, Y. Design of L-Shaped Open-Slot Antenna Used in UAV Airborne Communication System. *Int. J. Antennas Propag.* **2018**, *2018*, 6846193. [[CrossRef](#)]
39. Huang, Y.-H.; Wang, Y.; Zou, Y.-L.; Guo, J.-L. A Miniature Circularly Polarized Air-Borne Antenna With Wide Angle Coverage. *IEEE Antennas Wirel. Propag. Lett.* **2017**, *16*, 497–500. [[CrossRef](#)]
40. Yang, X.; Qi, Y.; Yuan, B.; Cao, Y.; Wang, G.; Casula, G.A. A Miniaturized High-Gain Flexible Antenna for UAV Applications. *Int. J. Antennas Propag.* **2021**, *2021*, 9919425. [[CrossRef](#)]
41. Agnessens, S.; Rogier, H. Compact Half Diamond Dual-Band Textile HMSIW On-Body Antenna. *IEEE Trans. Antennas Propag.* **2014**, *62*, 2374–2381. [[CrossRef](#)]

42. Velan, S.; Sundarsingh, E.F.; Kanagasabai, M.; Sarma, A.K.; Raviteja, C.; Sivasamy, R.; Pakkathillam, J.K. Dual-Band EBG Integrated Monopole Antenna Deploying Fractal Geometry for Wearable Applications. *IEEE Antennas Wirel. Propag. Lett.* **2015**, *14*, 249–252. [[CrossRef](#)]
43. Moscato, S.; Bahr, R.; Le, T.; Pasian, M.; Bozzi, M.; Perregrini, L.; Tentzeris, M.M. Infill-Dependent 3-D-Printed Material Based on NinjaFlex Filament for Antenna Applications. *IEEE Antennas Wirel. Propag. Lett.* **2016**, *15*, 1506–1509. [[CrossRef](#)]
44. Smida, A.; Iqbal, A.; Alazemi, A.J.; Waly, M.I.; Ghayoula, R.; Kim, S. Wideband Wearable Antenna for Biomedical Telemetry Applications. *IEEE Access* **2020**, *8*, 15687–15694. [[CrossRef](#)]
45. Abhinav, K.V.; Rao, R.V.K.; Karthik, P.S.; Singh, S.P. Copper conductive inks: Synthesis and utilization in flexible electronics. *RSC Adv.* **2015**, *5*, 63985–64030. [[CrossRef](#)]
46. Lamminen, A.; Arapov, K.; de With, G.; Haque, S.; Sandberg, H.G.O.; Friedrich, H.; Ermolov, V. Graphene-Flakes Printed Wideband Elliptical Dipole Antenna for Low-Cost Wireless Communications Applications. *IEEE Antennas Wirel. Propag. Lett.* **2017**, *16*, 1883–1886. [[CrossRef](#)]
47. Rizwan, M.; Khan, M.W.A.; Sydanheimo, L.; Virkki, J.; Ukkonen, L. Flexible and Stretchable Brush-Painted Wearable Antenna on a Three-Dimensional (3-D) Printed Substrate. *IEEE Antennas Wirel. Propag. Lett.* **2017**, *16*, 3108–3112. [[CrossRef](#)]
48. Abutarboush, H.F.; Li, W.; Shamim, A. Flexible-Screen-Printed Antenna With Enhanced Bandwidth by Employing Defected Ground Structure. *IEEE Antennas Wirel. Propag. Lett.* **2020**, *19*, 1803–1807. [[CrossRef](#)]
49. Sreelekshmi, S.; Perumal Sankar, S. A square ring and single split resonator based wearable antenna for Microwave energy harvesting for IoT nodes. *Sustain. Energy Technol. Assess.* **2022**, *52*, 102217. [[CrossRef](#)]
50. El-Hameed, A.S.A.; Salem, D.A.; Abdallah, E.A. Ultra Wide Band CPW-Fed Circularly Polarized Square Slot Antenna. In Proceedings of the 2013 IEEE Antennas and Propagation Society International Symposium (APSURSI), Orlando, FL, USA, 7–13 July 2013; p. 2. [[CrossRef](#)]
51. Qiao, X.; Geng, W.; Chen, X.; Zhang, L.; Zheng, D.; Zhang, L.; He, J.; Hou, X.; Yang, Y.; Cui, M.; et al. Enhanced energy storage properties and temperature stability of fatigue-free La-modified PbZrO<sub>3</sub> films under low electric fields. *Sci. China Mater.* **2020**, *63*, 2325–2334. [[CrossRef](#)]
52. Qiao, X.; Geng, W.; Sun, Y.; Yu, J.; Chen, X.; Yang, Y.; Cui, M.; Hou, X.; Zeng, K.; Chou, X. Preparation of high piezoelectric and flexible polyvinylidene fluoride nanofibers via lead zirconium titanate doping. *Ceram. Int.* **2020**, *46*, 28735–28741. [[CrossRef](#)]
53. Li, J.; Jiang, Y.; Zhao, X. Circularly Polarized Wearable Antenna Based on NinjaFlex-Embedded Conductive Fabric. *Int. J. Antennas Propag.* **2019**, *2019*, 3059480. [[CrossRef](#)]
54. Sayem, A.S.M.; Simorangkir, R.B.V.B.; Esselle, K.P.; Hashmi, R.M. Development of Robust Transparent Conformal Antennas Based on Conductive Mesh-Polymer Composite for Unobtrusive Wearable Applications. *IEEE Trans. Antennas Propag.* **2019**, *67*, 7216–7224. [[CrossRef](#)]
55. Sayem, A.S.M.; Simorangkir, R.B.V.B.; Esselle, K.P.; Lalbakhsh, A.; Gawade, D.R.; O’Flynn, B.; Buckley, J.L. Flexible and Transparent Circularly Polarized Patch Antenna for Reliable Unobtrusive Wearable Wireless Communications. *Sensors* **2022**, *22*, 1276. [[CrossRef](#)] [[PubMed](#)]
56. Awang, Z.; Affendi, N.A.M.; Alias, N.A.L.; Razal, N.M. Flexible Antennas Based on Natural Rubber. *Prog. Electromagn. Res. C* **2016**, *61*, 75–90. [[CrossRef](#)]
57. Althwayb, A.A.; Alibakhshikenari, M.; Virdee, B.S.; Rashid, N.; Kaaniche, K.; Atitallah, A.B.; Armghan, A.; Elhamrawy, O.I.; See, C.H.; Falcone, F. Metasurface-Inspired Flexible Wearable MIMO Antenna Array for Wireless Body Area Network Applications and Biomedical Telemetry Devices. *IEEE Access* **2023**, *11*, 1039–1056. [[CrossRef](#)]
58. Bolaños-Torres, M.Á.; Torrealba-Meléndez, R.; Muñoz-Pacheco, J.M.; Gómez-Pavón, L.d.C.; Tamariz-Flores, E.I. Multiband Flexible Antenna for Wearable Personal Communications. *Wirel. Pers. Commun.* **2018**, *100*, 1753–1764. [[CrossRef](#)]
59. Ullah, M.; Islam, M.; Alam, T.; Ashraf, F. Paper-Based Flexible Antenna for Wearable Telemedicine Applications at 2.4 GHz ISM Band. *Sensors* **2018**, *18*, 4214. [[CrossRef](#)]
60. Haagenson, T.; Noghianian, S.; de Leon, P.; Chang, Y.-h. Textile Antennas for Spacesuit Applications: Design, simulation, manufacturing, and testing of textile patch antennas for spacesuit applications. *IEEE Antennas Propag. Mag.* **2015**, *57*, 64–73. [[CrossRef](#)]

**Disclaimer/Publisher’s Note:** The statements, opinions and data contained in all publications are solely those of the individual author(s) and contributor(s) and not of MDPI and/or the editor(s). MDPI and/or the editor(s) disclaim responsibility for any injury to people or property resulting from any ideas, methods, instructions or products referred to in the content.